2

Dynamic Elastic Electron Scattering I: Bloch Wave Theory

The kinematic scattering theory illustrated in Chapter 1 holds only for crystals thinner than about 2 nm (Hoerni, 1956). The general characteristics, such as the positions of Bragg beams, can be precisely determined by the kinematic theory. The intensity of each reflection, however, is largely affected by multiple scattering effects among existing beams, because the interaction between the electron and the crystal is so strong that multiple-scattering effects are unavoidable. Therefore quantitative data analysis has to be performed based on dynamic scattering calculations. For this reason, the present and following chapters are devoted to the dynamic scattering behavior of electrons.

Diffraction theories of high-energy electrons have been established for many years. One of the most classical approaches is the Bloch wave theory, proposed by Bethe (1928). This theory has taken a dominant role in calculating convergent beam electron diffraction (CBED) and diffraction contrast imaging. In Chapter 2, the Bloch wave is introduced and its general properties are illustrated. Some simplified cases are discussed to illustrate applications of the theory. Finally the theory is extended to imperfect crystals.

2.1. RELATIVISTIC CORRECTIONS IN SINGLE-ELECTRON SCATTERING THEORY

Based on the first principles approach, we consider the fundamental equation that governs high-energy electron scattering in crystals. Before we show the mathematical description, it is important to consider the nature of the events we are studying. The average distance between successive electrons that strike the crystal in a TEM is about 0.2 mm (for 100-keV electrons) if the electron flux is on the order of 10^{12} e/s. This distance is much larger than the thickness (typically less than 0.5

μm) of the specimen; thus the interaction between successive incident electrons is extremely weak. Therefore interaction between the incident beam and the crystal can be treated as a case of one electron a time. In other words, electron diffraction theory is basically a single-electron scattering theory. The entire discussion of this book is based on this assumption.

Strictly speaking, high-energy electron scattering obeys the Dirac equation. The Dirac equation contains not only the relativistic effects but also electron spin. It has been shown by Fujiwara (1961) and Howie (1962) that electron spin is negligible in transmission electron diffraction, but relativistic corrections in the electron mass and wavelength have to be considered in both kinematic and dynamic scattering theories (see Gevers and David, 1982, for a review). In general, the solution of the Dirac equation for high-energy electron diffraction is quite complex (Fujiwara, 1961). We intend to derive a relativistically corrected Schrödinger-like equation. The solution of the equation should be sufficient for accuracy in quantitative electron microscopy. The relativistic energy momentum conservation equation for an electron accelerated to a kinetic energy of $e(U_0 + V)$ is

$$W^2 = p^2c_0^2 + m_0^2c_0^4 = [e(U_0 + V) + m_0c_0^2]^2 \tag{2.1a}$$

and

$$W = m_ec_0^2 = \frac{m_0c_0^2}{[1 - (v/c_0)^2]^{1/2}} = e(U_0 + V) + m_0c_0^2 \tag{2.1b}$$

where V is the electrostatic potential field of the crystal and c_0 is the speed of light. Neglecting the V^2 term, combining Eqs. (2.1a–b) yields

$$p^2c_0^2 - 2m_ec_0^2eV \approx eU_0(eU_0 + 2m_0c_0^2) \tag{2.2}$$

Replacing p by the operator $-i\hbar\nabla$ and applying Eq. (2.2) on Ψ, a Schrödinger-like equation (Humphreys, 1979; Spence, 1988a) is derived

$$-\frac{\hbar^2}{2m_0}\nabla^2\Psi - \gamma eV\Psi = E\Psi \tag{2.3}$$

where

$$E = eU_0[1 + \frac{eU_0}{2m_0c_0^2}]$$

and the relativistic factor $\gamma = m_e/m_0$. E is electron energy with relativistic correction. Therefore under the first-order approximation, the Schrödinger equation can be used to describe high-energy electron scattering if relativistic corrections are properly considered. For $V = 0$, the free-space solution of Eq. (2.3) gives exactly

the same wavelength as that originally based on de Broglie's relation in Eq. (1.3). By defining an effective crystal potential

$$U(\mathbf{r}) = \frac{2\gamma m_0e}{h^2}V(\mathbf{r}) \tag{2.4a}$$

and the electron wave number as

$$K = \frac{(2m_0E)^{1/2}}{h} \tag{2.4b}$$

Eq. (2.3) is rewritten as

$$\{\nabla^2 + 4\pi^2[U(\mathbf{r}) + K^2]\}\Psi(\mathbf{r}) = 0 \tag{2.5}$$

This is the fundamental equation that governs the scattering behavior of electrons in crystals. Discussions in Chapters 2–5 show how to solve this equation using various methods.

2.2. BETHE THEORY

2.2.1. Basic Equations

The solution of Eq. (2.5) was first given by Bethe (1928). The full solution is written as a linear superposition of Bloch waves

$$\Psi(\mathbf{r}) = \sum_i \alpha_iB_i(\mathbf{r}) \tag{2.6}$$

each Bloch wave $B_i(\mathbf{r})$ is an eigen solution of Eq. (2.5), and coefficients α_i are determined by boundary conditions. Equation (2.6) means that each Bloch wave is an eigenstate of the electron crystal system, and the electron wave function is a linear superposition of Bloch waves. The probability that the ith Bloch wave is excited is determined by the superposition coefficient α_i. Although there are many Bloch wave states in the crystal, boundary conditions determine which waves are excited. This is similar to the selection of Bragg beams by the diffracting condition in electron diffraction. Even though there are many possible Bragg reflections, those in the diffraction pattern are selected by the initial diffracting condition, as illustrated by the Ewald sphere in Fig. 1.7.

The Bloch wave theory is usually convenient for examining the diffraction of a periodically structured crystal. In this case, the modified crystal potential U can be expanded as a Fourier series based on reciprocal lattice vectors,

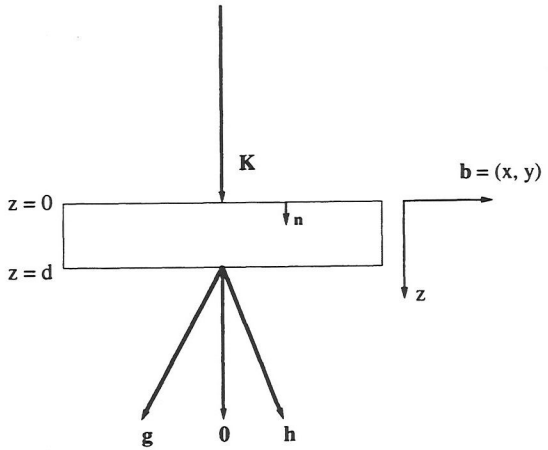

Figure 2.1. The coordinate system used in describing the transmission electron diffraction.

$$U(\mathbf{r}) = \sum_g U_g \exp(2\pi i \mathbf{g}\cdot\mathbf{r}) \tag{2.7a}$$

with

$$U_g = \frac{2\gamma m_0 e}{h^2} \sum_\alpha V_g \exp(-2\pi i \mathbf{g}\cdot\mathbf{r}_\alpha) \tag{2.7b}$$

Similarly the Bloch wave within the crystal may also be written as a Fourier series

$$B(\mathbf{r}) = \sum_g C_g \exp[2\pi i(\mathbf{k}+\mathbf{g})\cdot\mathbf{r}] \tag{2.8}$$

where C_g is the Bloch wave coefficient for Bragg reflection **g**. For high-energy electron diffraction, a Bloch wave is neither a spherical wave nor a single plane wave but a linear superposition of plane waves with wave vectors (**k** + **g**). A Bloch wave contains many plane wave components.

Equation (2.8) is introduced to convert a second-order differential equation into a set of linear algebra equations whose solution can easily be obtained from matrix diagonalization. Substituting Eqs. (2.7) and (2.8) into Eq. (2.5) yields

$$\sum_g \{[K^2 - (\mathbf{k}+\mathbf{g})^2]C_g + \sum_h U_{g-h}C_h\} \exp[2\pi i(\mathbf{k}+\mathbf{g})\cdot\mathbf{r}] = 0 \tag{2.9}$$

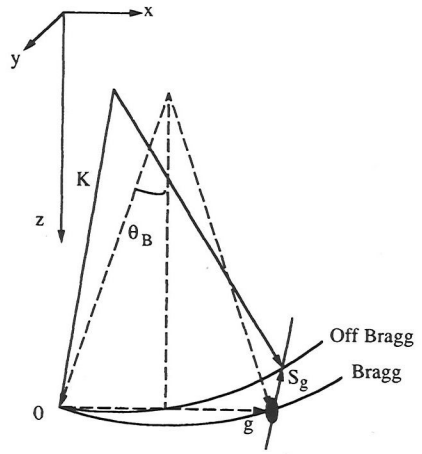

Figure 2.2. The Ewald sphere construction of electron diffraction at on-Bragg (*dashed lines*) and off-Bragg (*solid lines*) conditions. The excitation error S_g is indicated.

where **h** is the reciprocal lattice vector and the interaction between **g** and **h** beams is determined by U_{g-h}. Equation (2.9) holds for all **r** in the crystal. Hence the coefficient of each exponential term must be zero. For the **g** reflection,

$$[K^2 - (\mathbf{k}+\mathbf{g})^2]C_g + \sum_h U_{g-h}C_h = 0 \tag{2.10a}$$

Equation (2.10a) is actually a set of coupled equation for different **g** reflections. By choosing

$$\mathbf{k} = \mathbf{K} + \nu\mathbf{n} \tag{2.10b}$$

where **n** is a unit vector inward and normal to the crystal slab surface, as shown in Fig. 2.1. We have

$$[K^2 - (\mathbf{k}+\mathbf{g})^2] = 2KS_g - 2(\mathbf{K}+\mathbf{g})\cdot\mathbf{n}\nu - \nu^2 \tag{2.11a}$$

where the excitation errors S_g are defined as

$$2KS_g = K^2 - (\mathbf{K}+\mathbf{g})^2 \tag{2.11b}$$

The S_g is the distance from a reciprocal lattice point **g** to the intersection point of a line, drawn from **g** in parallel to **K**, with the Ewald sphere (see Fig. 2.2). The Bragg condition is defined by $S_g = 0$, which means the Bragg beam is located just on the surface of the Ewald sphere. By neglecting the ν^2 term for high-energy transmission electron diffraction (the error introduced by this approximation is very small according to Kim and Sheinin, 1982), substituting Eq. (2.11a) into (2.10a) yields

$$2KS_gC_g + \sum_h U_{g-h}C_h = 2(\mathbf{K}+\mathbf{g})\cdot\mathbf{n}\nu C_g \tag{2.12}$$

This is the fundamental equation of Bloch wave theory. Characteristics of Eq. (2.12) are discussed in the next section.

2.2.2. Characteristics of Bloch Waves

We now consider transmission electron diffraction (i.e., the Laue case) by assuming that all the **g**s lie in a plane perpendicular to **n**, i.e., $\mathbf{g}\cdot\mathbf{n} = 0$. This condition restricts the following solution to the ZOLZ reflections if **n** is antiparallel to the z axis. Equation (2.12) can readily be written as

$$2KS_gC_g + \sum_h U_{g-h}C_h = 2\mathbf{K}\cdot\mathbf{n}\nu\, C_g \tag{2.13}$$

or expressed in a matrix form

$$\mathbf{A}C^{(i)} = 2K_n\nu_i\mathbf{C}^{(i)} \tag{2.14}$$

where elements of the **A** matrix are $A_{gh} = 2KS_g\delta_{gh} + U_{g-h}$ and $K_n = \mathbf{K}\cdot\mathbf{n}$. If m beams are considered in the scattering, **A** is an $(m\times m)$ matrix, and there are m eigenvalues ν_i and m Bloch waves, each Bloch wave having m plane wave components. Equation (2.14) is just an eigen equation of $C_g^{(i)}$ with eigenvalue ν_i. Each eigen solution gives the superposition coefficients $C_g^{(i)}$ of the ith Bloch wave. The number of Bloch waves equals the number of beams or the dimension of the **C** matrix.

The set of equations represented by Eq. (2.12) is exact provided an infinite number of **g** values is considered. In practice the number of beams can be reduced depending on the required accuracy of numerical calculations.

Since $U(\mathbf{r})$ is real for elastic scattering without absorption, its Fourier coefficients satisfy $U_g = U_{-g}^*$, and the matrix **A** is thus Hermitian. Hence the eigenvalues ν_i are real (Landau and Lifshitz, 1977), although the eigenvectors $\mathbf{C}^{(i)}$ are, in general, complex. The eigenvector **C** matrix is unitary (Rez, 1976; Humphreys, 1979), i.e., the inverse of **C** is the complex conjugate and the transpose of **C**

$$\mathbf{C}^{-1} = \mathbf{C}^{+} \tag{2.15}$$

Explicitly writing this equation yields

$$\sum_i C_g^{(i)}C_h^{(i)*} = \delta_{g,h} \tag{2.16a}$$

and

$$\sum_g C_g^{(i)}C_g^{(j)*} = \delta_{i,j} \tag{2.16b}$$

where superscriptions i and j are added to represent the ith and the jth Bloch waves. This means that eigenvectors form a complete orthonormal set if the crystal potential is a real function. The following relations also hold among the eigenvectors and eigenvalues (Fukuhara, 1966; Spence, 1988a):

$$C_g^{(i)}(\mathbf{k}+\mathbf{h}) = C_g^{(i)}(\mathbf{k}) \tag{2.16c}$$

$$\nu_i(\mathbf{k}+\mathbf{h}) = \nu_i(\mathbf{k}) + S_h \tag{2.16d}$$

and

$$C_g^{(i)}(\mathbf{k}) = C_{-g}^{(i)*}(\mathbf{k}) \tag{2.16e}$$

A comprehensive description of the symmetry of Bloch waves is given by Gjønnes and Taftø (1993).

We now determine the superpersition coefficients α_i of Bloch waves. The α_i coefficients are easily obtained only if the incident wave is a plane wave. In the Laue case, the boundary condition at $z = 0$ requires $\Psi(\mathbf{K},\mathbf{b}) = \exp[2\pi i\mathbf{K}\cdot\mathbf{b}]$ or

$$\sum_i \alpha_i \sum_g C_g^{(i)} \exp[2\pi i(\mathbf{K}+\mathbf{g})\cdot\mathbf{r}] = \exp[2\pi i\mathbf{K}\cdot\mathbf{b}]$$

This equation is satisfied if $\alpha_i = C_0^{(i)*}$, considering the orthonormal relationship in Eq. (2.16a). Thus Eq. (2.6) becomes

$$\Psi(\mathbf{K},\mathbf{r}) = \sum_i C_0^{(i)*}\, B_i(\mathbf{r}) \tag{2.17a}$$

with

$$B_i(\mathbf{r}) = \sum_g C_g^{(i)} \exp[2\pi i(\mathbf{K}+\mathbf{g})\cdot\mathbf{r} + 2\pi i\nu_i z] \tag{2.17b}$$

where the direction of the z axis is parallel to the direction of the incident beam. It is important to point out that the Bloch wave solution introduced in Eq. (2.17) can be applied to calculate only the diffraction of a plane wave. Separated calculations are required if the incident electron probe is a superposition of plane waves.

2.2.3. Orthonormal Relationship of Bloch Waves

For Laue reflections with **g** lying in the x-y plane, i.e., $g_z = 0$, we now prove the orthonormal relation of the Bloch waves. From Eq. (2.17b),

$$\int d\mathbf{r}\, B_i^*(\mathbf{r})\, B_j(\mathbf{r}) = \sum_{gh} C_g^{(i)*}\, C_h^{(j)} \int d\mathbf{r} \exp[2\pi i(\mathbf{h}-\mathbf{g})\cdot\mathbf{b} + 2\pi i(\nu_j - \nu_i)z]$$

$$= \sum_{g} C_g^{(i)*}\, C_g^{(j)} \int dz \exp[2\pi i(\nu_j - \nu_i)z] = \delta_{i,j} \tag{2.18}$$

This means that Bloch waves are an orthonormal set. But this orthogonal relation holds only in the symmetric Laue case (i.e., $g_z = 0$ for the ZOLZ) under the approximation of high energy (Kim and Sheinin, 1987). In this case, the orthonormal relation holds regardless of whether the Bloch function is degenerate or nondegenerate. Thus the solution of the Schrödinger equation can usually be expanded as a linear superposition of Bloch waves. For a general case with $g_z \neq 0$, two Bloch functions are orthogonal if $\nu_j \neq \nu_i$. If $\nu_j = \nu_i$, however, the two Bloch functions may not be orthogonal. The orthonormal relation of the Bloch waves is useful in solving the Green function solution of the Schrödinger equation for a point electron emitter (see Chapter 10).

2.2.4. Bethe Theory and Band Structure Theory

Bethe's theory for electron diffraction is closely related to the energy band concept in the electronic theory of solids, since both represent the electronic state in terms of Bloch functions (Kambe and Moliere, 1970). Morse (1930) pointed out the close connection between the two theories and demonstrated that the Bragg peaks observed in low-energy electron diffraction occur in energy ranges that are forbidden by the band structure of the crystal. For high-energy electron diffraction, the two theories may be compared with each other in the following respects:

In band structure theory, Bloch functions are regarded as representing stationary states of valence electrons in a crystal. The propagation vector $\mathbf{k}$ is given as a parameter, and the eigenvalue of the energy $E(\mathbf{k})$ is calculated as a function of $\mathbf{k}$. In Bethe's theory, on the other hand, Bloch functions are used to construct the wave function of the scattered electron inside the crystal, given the energy of the incident electrons. Thus the dispersion surface is an equal energy surface in reciprocal space similar to the Fermi surface in band theory.

In band theory, using the Hartree approximation, the potential is defined as the average Coulomb potential due to the nuclei, the ion core electrons, and all the valence electrons except the one valence electron under consideration. In this case, the exchange and correlation effects between the electron under consideration and all other electrons are not negligible, and thus these affect the Hartree potential. For electron diffraction, however, the Bethe theory states that the potential is due to the

nuclei and all electrons belonging to the crystal, and it is not affected by incident electrons.

In band theory, the plane wave expansion of the Bloch function is usually poorly convergent, especially near the nuclei where the wave function varies rapidly. In the Bethe theory for electron diffraction, the convergence of the plane wave expansion is usually sufficiently rapid. In general, the number of plane waves is the number of beams in the diffraction pattern.

2.3. TWO-BEAM THEORY

The most important advantage of the Bloch wave approach is its clarity when describing the excitation of each Bloch wave. We now consider a case in which only two beams are involved. Equation (2.14) becomes

$$\begin{pmatrix} -2K_n\nu & U_{-g} \\ U_g & 2KS_g - 2K_n\nu \end{pmatrix} \begin{pmatrix} C_0 \\ C_g \end{pmatrix} = 0 \tag{2.19}$$

The eigenvalues ν are obtained by setting the determinant of the matrix equal to zero, thus leading to the following solutions:

$$\nu_{1,2} = \frac{\{KS_g \pm [(KS_g)^2 + |U_g|^2]^{1/2}\}}{2K_n} \tag{2.20a}$$

where superscript 1 refers to + and 2 to –. The difference of $\nu_1 - \nu_2$ is

$$\Delta\nu = \nu_1 - \nu_2 = \frac{[(KS_g)^2 + |U_g|^2]^{1/2}}{K_n} \tag{2.20b}$$

which corresponds to the gap between the two dispersion surfaces; this is discussed later in Chapter 2. If we set

$$w = \frac{KS_g}{|U_g|} = S_g\xi_g$$

where $\xi_g = K/U_g$ is the extinction distance, the ratio of C_0 and C_g can be found from Eq. (2.19)

$$\left[\frac{C_g}{C_0}\right]^{(1,2)} = w \pm (1 + w^2)^{1/2} \tag{2.20c}$$

By defining $\gamma_0 = \text{arcctg}\, w$ and considering the normalization relation $|C_0|^2 + |C_g|^2 = 1$, the Bloch wave coefficients are

$$C_0^{(1)} = C_g^{(2)} = \cos(\gamma_0/2) \tag{2.21a}$$

and

$$C_0^{(1)} = -C_g^{(2)} = \sin(\gamma_0/2) \tag{2.21b}$$

corresponding to Bloch waves of

$$B_1(\mathbf{r}) = \exp(2\pi i\mathbf{K}\cdot\mathbf{r} + 2\pi i v_1 z)[\cos(\gamma_0/2) + \sin(\gamma_0/2)\exp(2\pi i\mathbf{g}\cdot\mathbf{r})] \tag{2.21c}$$

and

$$B_2(\mathbf{r}) = \exp(2\pi i\mathbf{K}\cdot\mathbf{r} + 2\pi i v_2 z)[\sin(\gamma_0/2) - \cos(\gamma_0/2)\exp(2\pi i\mathbf{g}\cdot\mathbf{r})] \tag{2.21d}$$

The two Bloch waves under the two-beam approximation are useful in qualitatively illustrating the physics involved in some imaging and diffraction processes. Substituting Eq. (2.21) into Eq. (2.17), the intensity of the diffracted beam at the exit face, where $z = d$, is

$$I_g = \left|\sum_i C_0^{(i)*} C_g^{(i)} \exp(2\pi i v_i d)\right|^2 = \frac{|U_g|^2 \sin^2(\pi d\Delta v)}{(K_z\Delta v)^2} \tag{2.22a}$$

and

$$I_0 = 1 - I_g \tag{2.22b}$$

The oscillation of I_0 with the variation of specimen thickness d corresponds to thickness fringes observed in bright-field TEM images, as shown in Fig. 2.3a. The dark-field image of the same area (Fig. 2.3b) recorded using the g reflection shows complimentary contrast as expected theoretically. Two adjacent thickness fringes correspond to a thickness change of $\Delta d = 1/\Delta v = \xi_g/(1 + w^2)^{1/2}$, where ξ_g is g dependent. At the Bragg condition $w = 0$, $\Delta d = \xi_g$. This means that the extinction distance is the thickness variation between two adjacent thickness fringes under the Bragg reflection condition.

Using the two-beam theory, we now show the channeling effect in electron diffraction. For simplicity, we consider the expressions of Eqs. (2.21c) and (2.21d) under the Bragg condition (i.e., $w = 0$)

$$B_1(\mathbf{r}) = \frac{1}{\sqrt{2}}\exp(2\pi i\mathbf{K}\cdot\mathbf{r} + 2\pi i v_1 z)[1 + \exp(2\pi i\mathbf{g}\cdot\mathbf{r})]$$

$$= \sqrt{2}\cos(\pi\mathbf{g}\cdot\mathbf{r})\exp(2\pi i\mathbf{K}\cdot\mathbf{r} + 2\pi i v_1 z + \pi i\mathbf{g}\cdot\mathbf{r})$$

with

$$|B_1(\mathbf{r})|^2 = 2\cos^2(\pi\mathbf{g}\cdot\mathbf{r}) \tag{2.22c}$$

and

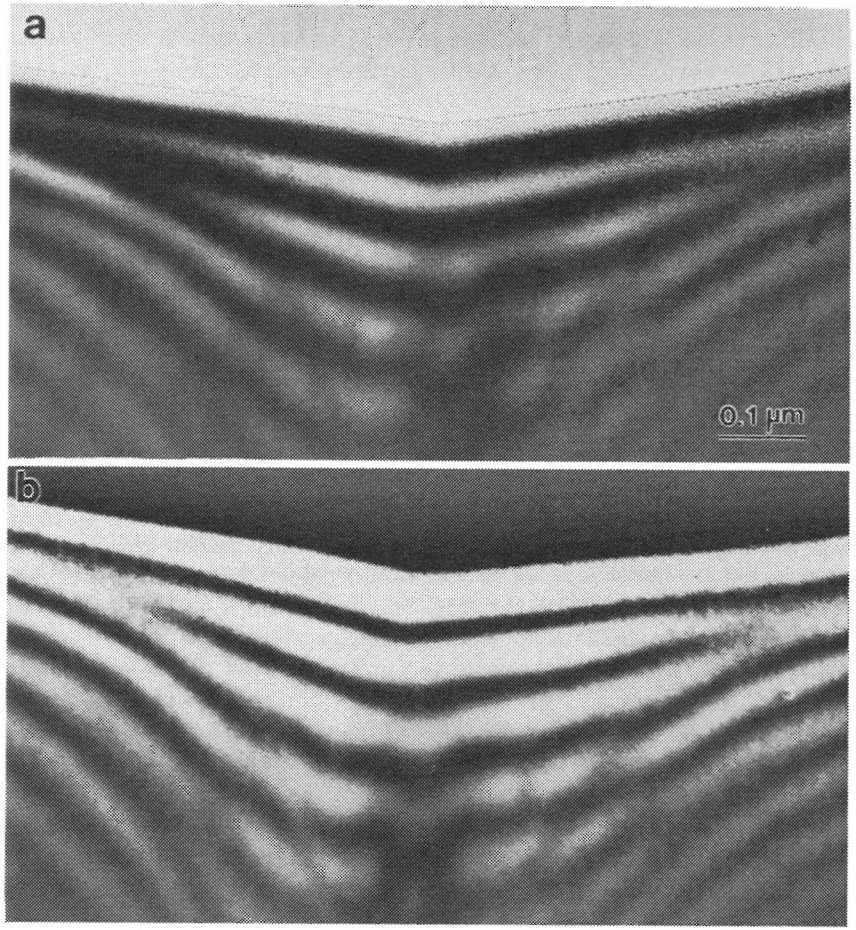

Figure 2.3. (a) Bright-field image and (b) g = (004) dark-field image of a thin silicon crystal oriented near the [100] zone, showing the thickness fringes. The contrast of the bright-field image is complimentary to that of the dark-field image. Beam energy is 100 keV.

$$B_2(\mathbf{r}) = \frac{1}{\sqrt{2}}\exp(2\pi i\mathbf{K}\cdot\mathbf{r} + 2\pi i v_2 z)[1 - \exp(2\pi i\mathbf{g}\cdot\mathbf{r})]$$

$$= i\sqrt{2}\sin(\pi\mathbf{g}\cdot\mathbf{r})\exp(2\pi i\mathbf{K}\cdot\mathbf{r} + 2\pi i v_2 z + \pi i\mathbf{g}\cdot\mathbf{r})$$

with

$$|B_2(\mathbf{r})|^2 = 2\sin^2(\pi\mathbf{g}\cdot\mathbf{r}) \tag{2.22d}$$

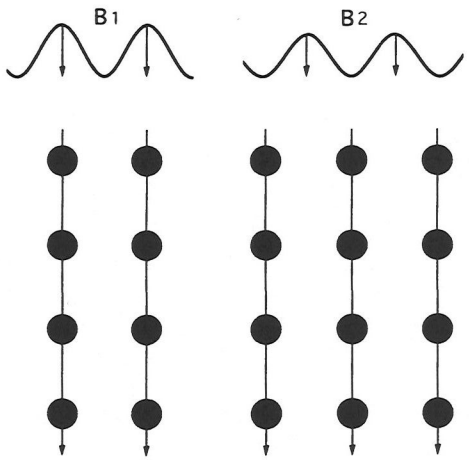

Figure 2.4. A schematic diagram of two types of Bloch wave fields under two-beam Bragg condition at the reflecting position in a simple cubic lattice. In both cases, the current flow vector (normal to the dispersion surface) is parallel to the reflecting planes. The B_1 wave is more strongly absorbed than B_2 due to a larger probability of inelastic excitation.

The electron current of each Bloch wave flows, on average, parallel to the Bragg planes, but it is modulated across the atom planes, so that for Bloch wave $B_2(\mathbf{r})$ the maximum occurs between the atomic planes (Fig. 2.4). For Bloch wave $B_1(\mathbf{r})$, the situation is reversed, and the current is concentrated on the atom planes, i.e., a stronger channeling effect. The channeling propagation of Bloch wave $B_1(\mathbf{r})$ along atom planes effectively increases the probability of inelastic excitations of the atomic inner shells, resulting in a stronger absorption effect (see Chapter 6).

The channeling effect illustrated here has many important applications in imaging of inelastically scattered electrons (see Chapter 11). Electron channeling along the paths of lowest potential energy (i.e., atomic rows) in crystal enhances the excitations of X-rays and Auger electrons in the atomic rows. The X-ray signals from impurity atoms located within certain crystal planes can be maximized if proper diffracting (or channeling) conditions are set up. This technique is known as atom location by channeling enhanced microanalysis (ALCHEMI) (see Spence, 1992, for a review).

Equation (2.22a) can be used to estimate the maximum crystal thickness smaller than which the kinematic scattering (or single-scattering) approximation holds (Hoerni, 1956). The scattering amplitude of the **g** beam under the kinematic scattering approximation increases linearly with increasing crystal thickness d. In

other words, the diffracted intensity increases with d^2. For simplicity, we start with Eq. (2.22a), assuming Bragg conditions, so that $I_g \approx \sin^2(\pi d/\xi_g)$. For small thickness satisfying $\pi d/\xi_g << 1$

$$I_g = \left(\frac{\pi d}{\xi_g}\right)^2 = \left(\frac{\pi d U_g}{K}\right)^2$$

as expected from kinematic scattering theory. For low-index reflections, the extinction distance ξ_g is a few tens of nanometers. Therefore for kinematic scattering theory to hold, $d << \xi_g/\pi$. In this thickness range, electron scattering can be approximately considered the result of single scattering, so that the high-resolution transmission electron microscopy (HRTEM) images of thin crystals are referred to structural images, from which positions of atoms may be directly identified from the image. For crystals with larger thicknesses, multiple scattering effects disturb the localized distribution of the incident electrons, so that the cross scattering of the electrons complicates the image interpretation. In this case, image simulation becomes indispensable.

A more sophisticated two-beam theory has also been derived for wedge-shaped and finite polyhedron crystals (Kato, 1952). The major task involved in irregular-shaped crystals is to match the solutions at the boundary. This can be easily done for the two-beam case, but the situation may become very complex if a many-beam theory is involved.

The theory developed here applies to purely elastically scattered electrons without absorption. Inelastic scattering during electron diffraction causes the incident electron to lose not only energy but also become angularly redistributed between Bragg beams. If the objective aperture is used to select one or more Bragg reflected beams to form an image, many of the inelastically scattered electrons are thus excluded from the image. These electrons are effectively absorbed. In general, the absorption effect is characterized by an imaginary potential in elastic-scattering calculations, and this effect decreases the intensity of Bragg-reflected beams. A systematic introduction of the imaginary potential is illustrated in Chapter 6.

2.4. DISPERSION SURFACES

The Bloch wave eigenvalues ν_i given by Eq. (2.20) depend on both the crystal-scattering potential (U_g) and the incident electron wave vector. For specific reflections with known U_gs, a relationship between the incident electron wave number K and the Bloch wave eigenvalue ν is called the dispersion surface, which is formed by the locus of allowed wave vectors for all beams. All wave vectors inside the crystal are restricted to lie on the dispersion surfaces. Explicitly speaking,

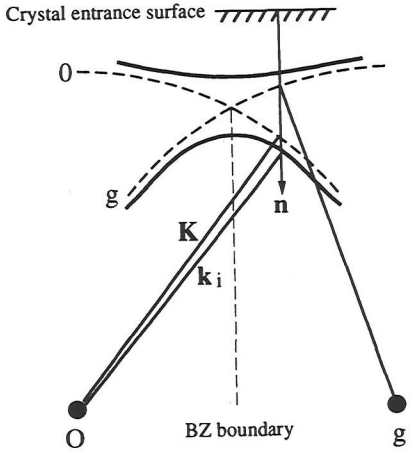

Figure 2.5. Dispersion surfaces under the two-beam approximation. Here v and S_g are measured in the direction of the surface normal **n**. The dashed curves 0 and g are parts of the Ewald spheres centered at O and **g**, respectively, with radius $K = 1/\lambda$.

the dispersion surface in electron diffraction is a plot of allowed values of the z component of the Bloch wave vector $k_z^{(i)}$ in the crystal. For simplification, we use dispersion relations for the two-beam case to illustrate the construction of dispersion surfaces.

We first consider the zero-order solution of Eq. (2.10a), where all Fourier coefficients U_{g-h} (for $\mathbf{g} \neq \mathbf{h}$) are switched off. Then $S_g = 0$, or $[\mathbf{k}^{(i)} + \mathbf{g}] = K^2$, and this describes a series of free-electron spheres of radius K centered at each of the reciprocal-lattice points **g** parallel to the surface (Whelan, 1986). One sphere is centered on the origin of reciprocal space and one centered on the reciprocal lattice point **g**, as shown in Fig. 2.5. These spheres intersect at the Brillouin zone boundary. A vector is drawn in the direction normal to the entrance surface of the crystal and intersecting the vector **K** at the sphere centered at O. The eigenvalues v_i are calculated from Eq. (2.20) using the actual U_g value. The values of v_i are measured along the surface normal direction, starting from a point on that K sphere that is centered at O. Thus the **K** vector must be drawn first. Then points on the dispersion surfaces are drawn at distances v_i measured from the end point of **K** along the surface normal direction **n**. The complete dispersion surfaces are obtained by repeating this procedure for each possible beam direction.

Two-beam diffraction is an ideal case in which the intensities of other beams are zero. In practice, this condition is rarely satisfied. The perturbation effect of weak beams can be reasonably included in the two-beam theory using the Bethe potential, which is discussed in Section 2.6. Further studies by Miyake (1959) and Gjønnes (1962a) indicated that the two-beam approximation fails to apply in the range of very short wavelength and small crystal thicknesses, even with the corrected dynamical Fourier potential. This is due to the increased radius of the

Ewald sphere, and the shape factor of the crystal for $\lambda \to 0$ (or $K \to \infty$) and $d \to 0$ result in many beam excitations.

2.5. APPLICATIONS IN CBED

The CBED patterns are formed with an electron probe focused on the sample, causing diffraction spots to broaden into disks. The incident probe consists of many plane wave components propagating along different directions, thus forming a converged conical electron probe, as shown in Fig. 2.6. For an incident beam P, the diffraction results in a complete point diffraction pattern consisting of Ps as ruled by the Bragg reflection law. A similar set of point diffraction patterns is formed for another plane wave component Q. Therefore for cases where there are no disk overlaps, a perfect registration is retained between each incident beam direction and the diffracted beams. The intensity profile across the diffracted disk **g** is called a rocking curve, which represents the variation of **g**-reflected intensity with the change of incident beam direction. Thus each point in the central (000) CBED disk corresponds to an incident plane wave component and defines a family of conjugate points differing by reciprocal lattice vectors, one in each CBED disk. The great power of the CBED techniques results from the fact that so much crystal structural information, such as crystal structure factors, charge density distribution, symmetry, strains, unit-cell parameters, and specimen thickness, can be determined quantitatively from analyses of CBED patterns (see Spence and Zuo, 1992, and Cowley, 1993, for a review).

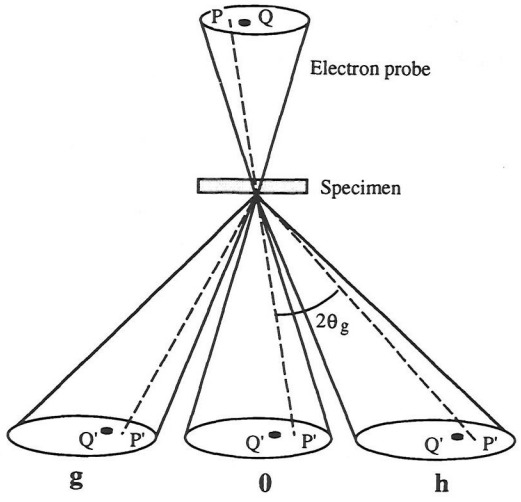

Figure 2.6. A schematic ray diagram of CBED. If only elastic Bragg scattering is allowed, then source point P gives rise to conjugate points P', one in each disk. Source point Q defines a different incident beam direction and set of diffracted beams Q'.

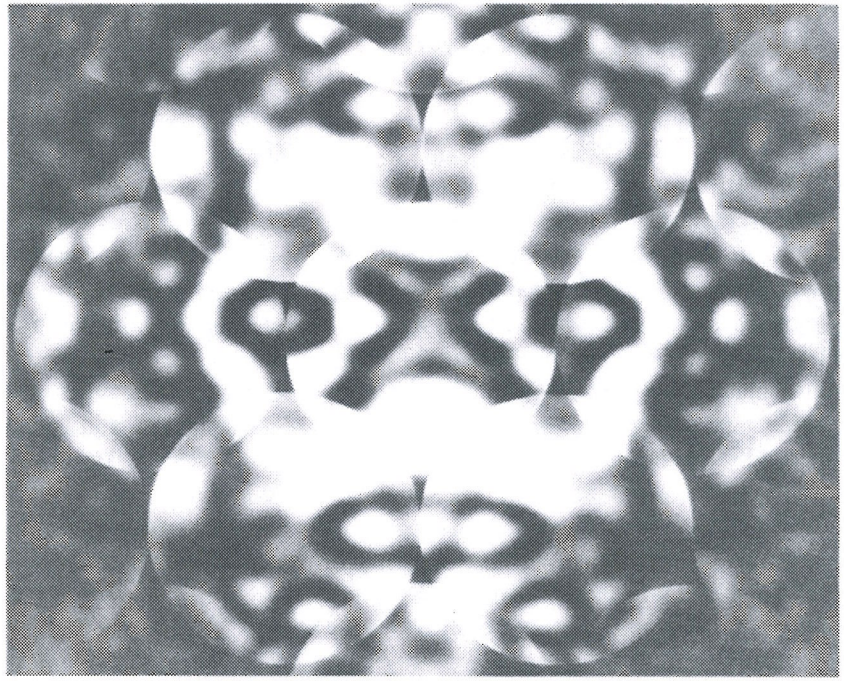

Figure 2.7. A CBED pattern of silicon viewed along [110] showing structural information contained in the pattern. The pattern was recorded at 100 keV.

Figure 2.7 shows a CBED pattern of [110] silicon. Fine details within each diffraction disk are the result of the dynamic diffraction of electrons entering the crystal from different directions. The symmetry of the intensity distribution indicates the projected central-symmetric and the (001) planar mirror-symmetric structure of the crystal. Quantification of the intensity distribution in reciprocal space is a powerful method for determining the crystal structure.

Calculating a rocking curve intensity profile in the angular ranges where there is no disk overlap is usually performed by the Bloch wave approach

$$I_g(\mathbf{K}) = \sum_i \sum_j C_0^{(i)*} C_g^{(i)} C_0^{(j)} C_g^{(j)*} \exp[2\pi i(\nu_i - \nu_j)d] \qquad (2.23a)$$

In CBED, many parameters are involved in the calculation of $I_g(\mathbf{K})$. Each of these parameters can be determined using different techniques. The specimen thickness is determined from thickness fringes in the diffraction disks under two-beam

conditions (Kelly et al., 1975). Unit-cell parameters can be determined by the position of HOLZ line positions in the center disk. Finally, crystal structure factors are refined from the rocking curves of different diffracting disks by comparing the calculated $I_g(\mathbf{K})$ with the experimentally measured I_g. An automated dynamic least-squares refinement program has been developed by Zuo and Spence (1991).

Figure 2.8 shows the experimentally observed zero energy loss CBED pattern (*dotted curve*) and the many-beam dynamic calculated (*solid line*) rocking curves for a BeO crystal (Spence and Zuo, 1992). The refinement of the calculated curve in comparison with the observed one yields low-index crystal structure factors. For the line scan across the (00n) systematic row, the amplitude and phase of the (002) structure factor at 80 kV are determined as

$$|U^{(R)}(002)| = 0.039592 \pm 0.00014 \text{ Å}^{-2}, \quad \varphi(002) = -0.88478 \pm 0.017 \text{ rad}$$

$$|U^{(I)}(002)| = 0.00073 \pm 0.00006 \text{ Å}^{-2}, \quad \varphi'(002) = -1.1 \pm 0.5 \text{ rad}$$

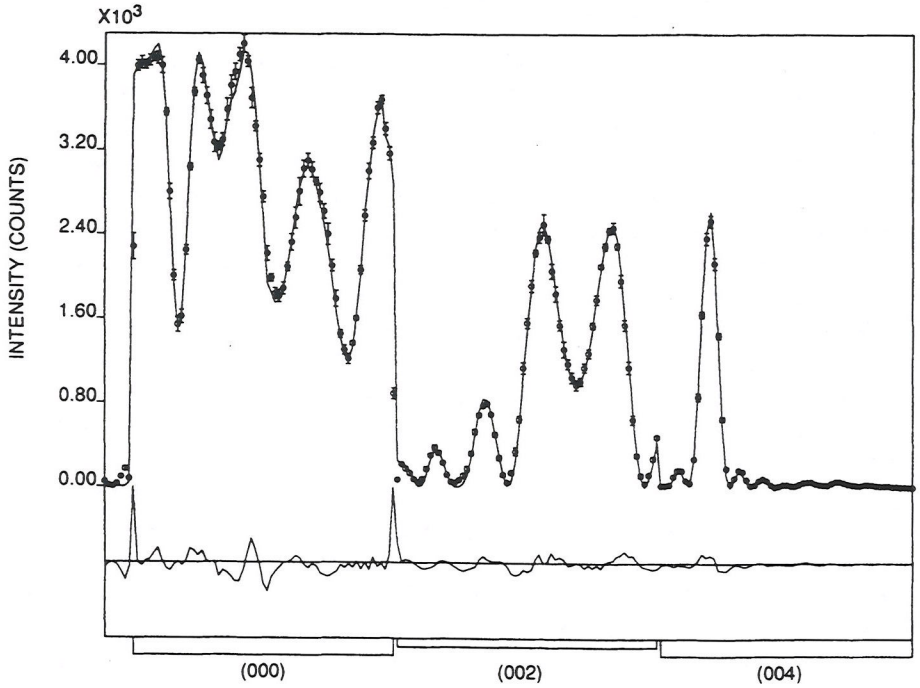

Figure 2.8. The zero energy loss experimental and computed CBED rocking curve along the (002) row of BeO at 80 kV. The (000), (002), and (004) disks are indicated. The crystal orientation is near the [130] zone axis. Specimen thickness d = 70.9 nm. The lower plot shows the difference between calculation and experiment. (Courtesy of Drs. J. C. H. Spence and J. M. Zuo, 1992)

and specimen thickness $d = 71.16$ nm.

If the bonding effect is ignored in a center-symmetric structure, and so that the atom potential is spherical symmetric, the structure factor U_g is a real function. However an imaginary component appears in U_g if the atomic potential is distorted by crystal bonding. Therefore the measurement of $U^{(I)}$ provides important information on charge redistribution in the crystal due to the solid-state effect. Quantitative CBED provides the most accurate method for measuring the charge redistribution of crystals smaller than a few hundred nanometers (Zuo et al., 1988).

If there are disk overlaps in CBED, calculations have to be performed separately for different incident beam directions in the overlapped regions, and the calculated amplitudes are then added coherently, incoherently, or partially coherently depending on the original assumption of the source coherence. For a perfectly coherent beam diffraction, especially if there are substantial disk overlaps, calculations using the multislice theory may be more convenient (see Chapter 3).

2.6. CRITICAL VOLTAGE EFFECT

The critical voltage effect is one of the typical examples of dynamic scattering in electron diffraction. If a crystal is set at the Bragg condition, normally the diffracted intensity is strong unless the crystal thickness is an integer number of extinction distances. This is due to the constructive interference of waves scattered in the diffracted beam direction. However for a particular incident electron-accelerating voltage, the so-called critical voltage U_{0c}, the diffracted beam intensity of a second-order reflection $2\mathbf{h}$ is very small for all thicknesses, due to destructive rather than constructive Bloch wave interference (Nagata and Fukuhara, 1967; Uyeda, 1968; Watenabe et al., 1968). This voltage depends sensitively on the ratio of first-to-second-order structure factors, and it is used to measure structure factors of low-order reflections that are particularly sensitive to bonding effects in crystals (for reviews, see Cowley, 1981; Humphreys, 1979; Reimer, 1984; Spence and Zuo, 1992).

As illustrated in Fig. 2.9, the critical voltage effect occurs at a three-beam diffracting condition, with $2\mathbf{h}$ in Bragg condition. This case can be treated either using three-beam theory or two-beam theory with the perturbation of a weak beam (Uyeda, 1968; Lally et al., 1972). For simplification, we start from the two-beam theory and consider the perturbation effect of other weak beams.

Discussions in Section 2.3 were based on an ideal two-beam case in which all other beams were assumed to have zero intensity. One way of including the weak beam effect is to use the perturbation theory of Bethe and rewrite Eq. (2.12) for symmetric Laue cases as

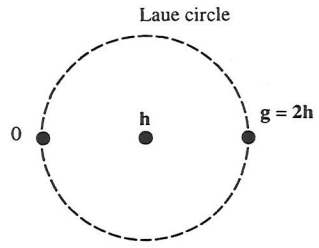

Figure 2.9. The three-beam diffracting condition for the critical voltage effect.

$$2KS_hC_h + \sum_{h'} U_{h-h'}C_{h'} = 2K_n\nu C_h \tag{2.23b}$$

where variable substitutations of $\mathbf{h}$ by $\mathbf{h}'$ and $\mathbf{g}$ by $\mathbf{h}$ were introduced. If $\mathbf{h}$ is a weak beam because $K|S_h| >> |U_g|$, Eq. (2.23b) can be solved for the two-beam case as

$$C_h = \frac{\sum_{h'} U_{h-h'}C_{h'}}{2KS_h - 2K_n\nu} \approx \frac{U_hC_0 + U_{h-g}C_g}{2KS_h} \tag{2.23c}$$

Substituting Eq. (2.23c) into (2.12) for the two-beam case, Eq. (2.19) is modified as

$$\begin{pmatrix} 2KS_0^{eff} - 2K_n\nu & U_{-g}^{eff} \\ U_g^{eff} & 2KS_g^{eff} - 2K_n\nu \end{pmatrix} \begin{pmatrix} C_0 \\ C_g \end{pmatrix} = 0 \tag{2.23d}$$

where

$$2KS_0^{eff} = -\sum_h \frac{|U_h|^2}{2KS_h} \quad 2KS_g^{eff} = 2KS_g - \sum_h \frac{|U_{g-h}|^2}{2KS_h}$$

and

$$U_g^{eff} = U_g - \sum_h \frac{U_hU_{g-h}}{2KS_h} \tag{2.24}$$

This effective structure factor is known as the Bethe potential. A more rigorous derivation using the Green's function has been given by Gjønnes (1962b).

We now apply Eqs. (2.24) to illustrate the critical voltage phenomenon, in which $\mathbf{g} = 2\mathbf{h}$ satisfies Bragg condition, and $\mathbf{h}$ is weak. For a minimum $\mathbf{g}$ reflection, we set $U_g^{eff} = 0$. This condition may be met by varying the accelerating voltage. Using the relation

$$U_{0c} = \frac{m_0 c_0^2(\gamma - 1)}{e} \tag{2.25}$$

solving γ from $U_g^{eff} = 0$ (Spence and Zuo, 1992) yields

$$U_{0c} = \frac{m_0 c_0^2}{e}\left(\frac{\hbar^2 g^2 V_{2h}}{2m_0 e V_h} - 1\right) \tag{2.26}$$

Equation (2.26) gives an approximate value of the critical voltage U_{0c} in terms of the two lowest order structure factors. If the second-order reflection is assumed to depend mainly on the single-atom scattering property, the first-order reflection, which is more sensitive to solid-state bonding effects, may be found with high precision using Eq. (2.26) (for a review, see Fox and Fisher, 1988). Accuracy of measurements is ultimately limited by the Debye–Waller factor for high-order reflection and the contrast of the intensity minimum at $2\mathbf{h}$.

2.7. DIFFRACTION OF LAYERED MATERIALS

The CBED techniques can be applied to study the strain, composition, and rigid-body displacements across layered materials (or quantum well materials). The Bloch wave theory developed in Section 2.2 can be extended to calculate the transmission electron diffraction pattern of layered materials (Rossouw et al., 1991; Peng and Whelan, 1990). We now consider a material composed of $m = 1$ to M layers, as shown in Fig. 2.10. The mth layer is located at $z = z_m$, with thickness d_m. For simplicity, we assume there is no rigid shift between the origins of the two adjacent layers. The wave function inside the mth layer is written as

$$\Psi_m(\mathbf{r}) = \sum_i \alpha_m^{(i)} \sum_{g_m} C_{g_m}^{(i)} \exp[2\pi i(\mathbf{K} + \mathbf{g}_m)\cdot\mathbf{r} + 2\pi i \nu_{im}(z - z_m)] \tag{2.27}$$

where ν_{im} and $C_{g_m}^{(i)}$ are the eigenvalues and eigenvectors, respectively, of the Bloch wave solution of the mth crystalline layer and $\mathbf{g}_m$ are the corresponding reciprocal lattice vectors. An analogous relation holds for the $(m+1)$th layer,

$$\Psi_{m+1}(\mathbf{r}) = \sum_i \alpha_{m+1}^{(i)} \sum_{g_{m+1}} C_{g_{m+1}}^{(i)} \exp[2\pi i(\mathbf{K} + \mathbf{g}_{m+1})\cdot\mathbf{r} + 2\pi i \nu_{m+1}(z - z_{m+1})] \tag{2.28}$$

Matching Eqs. (2.27) and (2.28) at the interface $z = z_{m+1}$ for the ZOLZ reflections and splitting $\mathbf{r} = (\mathbf{b}, z)$, we obtain

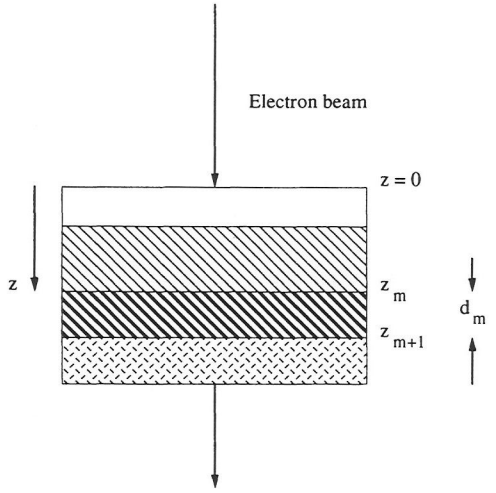

Figure 2.10. A schematic diagram showing layered structures along the beam direction.

$$\sum_i \alpha_{m+1}^{(i)} \sum_{g_{m+1}} C_{g_{m+1}}^{(i)} \exp(2\pi i \mathbf{g}_{m+1}\cdot\mathbf{b}) = \sum_i \alpha_m^{(i)} \sum_{g_m} C_{g_m}^{(i)} \exp(2\pi i \mathbf{g}_m\cdot\mathbf{b} + 2\pi i \nu_{im} d_m)$$

Multiplying this equation by $\exp(2\pi i \mathbf{h}_{m+1}\cdot\mathbf{b})$ and integrating over $\mathbf{b}$, we obtain

$$\sum_i \alpha_{m+1}^{(i)} C_{h_{m+1}}^{(i)} = \sum_i \alpha_m^{(i)} \sum_{g_m} C_{g_m}^{(i)} \delta(\mathbf{h}_{m+1} - \mathbf{g}_m) \exp(2\pi i \nu_{im} d_m)$$

Multiplying both sides by $C_{h_{m+1}}^{(i)*}$, summing over h_{m+1}, and using the orthonormal relation in Eq. (2.16b) yields

$$\alpha_{m+1}^{(j)} = \sum_i \alpha_m^{(i)} \sum_{g_m} \sum_{h_{m+1}} C_{g_m}^{(i)} C_{h_{m+1}}^{(j)*} \delta(\mathbf{h}_{m+1} - \mathbf{g}_m) \exp(2\pi i \nu_{im} d_m) \tag{2.29}$$

This relation correlates the superposition coefficients of the mth and $(m+1)$th layers. For $m = 1$, the boundary condition is satisfied by choosing $\alpha_1^{(j)} = C_0^{(j)*}$. Using Eq. (2.29), it is possible to determine the wave function inside each layer.

Two simple relations can be derived from Eq. (2.29). If the two adjacent layers have the same reciprocal lattice base vectors (i.e, same direction and same magnitude), then

$$\alpha_{m+1}^{(j)} = \alpha_m^{(j)} \exp(2\pi i \nu_{jm} d_m) \tag{2.30a}$$

If the two layers have different reciprocal lattice base vectors, so that $\mathbf{h}_{m+1} \neq \mathbf{g}_m$ unless $\mathbf{h}_{m+1} = 0$ and $\mathbf{g}_m = 0$, then

$$\alpha_{m+1}^{(j)} = \sum_i \alpha_m^{(i)} C_{0_m}^{(i)} C_{0_{m+1}}^{(j)*} \exp(2\pi i v_{im} d_m) \tag{2.30b}$$

Finally for a case where two adjacent layers have the same set of reciprocal lattice base vectors, a rigid shift $\Delta\mathbf{R}_m$ of the mth layer origin with respect to the origin of the $(m+1)$th layer may be incorporated into the calculation by multiplying the Bloch wave coefficients with a phase factor, i.e.,

$$C_{g_m}^{(i)} \rightarrow C_{g_m}^{(i)} \exp(-2\pi i \mathbf{g}_m \cdot \Delta\mathbf{R}_m) \tag{2.31a}$$

The preceding discussion makes it possible to apply the Bloch wave theory in calculating CBED patterns of layered materials if the incident beam is assumed to be perpendicular to the surface plane.

2.8. HOLZ REFLECTIONS

The theory outlined in the last few sections was based on an approximation of symmetric Laue cases for which $\mathbf{g}\cdot\mathbf{n} = 0$. This condition becomes $g_z = 0$ if the foil normal is antiparallel to the z axis; thus the theory is restricted to ZOLZ reflections. To include HOLZ reflections, we start from Eq. (2.12) by defining

$$B_g = (1 + \frac{g_n}{K_n})^{1/2} C_g \tag{2.31b}$$

where components normal to the crystal surface are $g_n = \mathbf{g}\cdot\mathbf{n}$, $h_n = \mathbf{h}\cdot\mathbf{n}$, and $K_n = \mathbf{K}\cdot\mathbf{n}$, so that Eq. (2.12) is rewritten as

$$\frac{2KS_g B_g}{1 + (g_n/K_n)} + \sum_h \frac{U_{g-h} B_h}{\{(1 + g_n/K_n)[1 + (h_n/K_n)]\}^{1/2}} = 2K_n \nu B_g \tag{2.31c}$$

This is a fundamental eigenvalue equation that includes all HOLZ effects and boundary inclination effects. The only approximation made in deriving Eq. (2.31c) is to ignore the ν^2 term for high-energy electron diffraction in the Laue case. The FORTRAN program provided by Spence and Zuo (1992) calculates Eq. (2.31), so that HOLZ reflections are automatically included.

2.9. REAL-SPACE BLOCH WAVE THEORY OF ZOLZ REFLECTIONS

The Bloch wave theory presented in the last few sections is essentially a reciprocal-space theory in which the differential equation was solved in reciprocal space. The dimension of the matrix is the number of beams involved in the calculation. The numerical calculation of this theory, however, may be quite involved especially for zone axis patterns in which many beams are involved. An alternative Bloch wave theory is thus introduced to solve the Schrödinger equation in real space (Howie, 1966; Berry, 1971; Buxton et al., 1978; Vincent et al., 1984; for a review, see Bird, 1989). This theory is particularly convenient for calculating zone-axis CBED patterns.

2.9.1. Projected Potential Approximation

Before we present the real-space Bloch wave theory, it is important to examine the portion of the crystal potential that is responsible for ZOLZ reflections. In zone-axis patterns, the dominant Bragg reflections are distributed within the ZOLZ. If $\mathbf{g}$ is written as $(\mathbf{g}_b, g_z)$, the crystal potential is written as

$$U(\mathbf{r}) = \sum_g U_g \exp(2\pi i \mathbf{g}\cdot\mathbf{r}) = \sum_g U_g \exp(2\pi i \mathbf{g}_b\cdot\mathbf{b} + 2\pi i g_z z)$$

$$= U^{(0)}(\mathbf{b}) + U^{(H)}(\mathbf{b},z) \tag{2.32a}$$

where

$$U^{(0)}(\mathbf{b}) = \sum_{g_b} U_{g_b} \exp(2\pi i \mathbf{g}_b\cdot\mathbf{b}) \tag{2.32b}$$

is the projected potential, and

$$U^{(H)}(\mathbf{r}) = \sum_{g_z \neq 0} \exp(2\pi i g_z z) \sum_{g_b} U_g \exp(2\pi i \mathbf{g}_b\cdot\mathbf{b}) \tag{2.32c}$$

which is the potential responsible for HOLZ reflections because $g_z \neq 0$. Therefore the diffraction of ZOLZ reflections is directly determined by the projected potential $U^{(0)}(\mathbf{b})$. This means that the ZOLZ approximation is the projected potential approximation; the projected potential approximation actually restricts the theory to the ZOLZ reflections only.

2.9.2. ZOLZ Reflections

Starting from the Schrödinger equation and factoring out the rapid variation in the z direction,

$$\Psi(\mathbf{r}) = \exp(2\pi i \mathbf{K}\cdot\mathbf{r})\, \Phi(\mathbf{b},z) \tag{2.33}$$

Substituting Eq. (2.33) into Eq. (2.5) gives

$$[\nabla_b^2 + 4\pi^2 U(\mathbf{r})]\Phi(\mathbf{b},z) \approx -4\pi i K_z \frac{\partial \Phi(\mathbf{b},z)}{\partial z} \tag{2.34}$$

where the ∇_b^2 operator acts only on the transverse coordinate $\mathbf{b}$; $\partial^2\Phi/\partial z^2$ was dropped under the small angle-scattering approximation; and $\partial\Phi(\mathbf{b},z)/\partial x$ and $\partial\Phi(\mathbf{b},z)/\partial y$ are neglected because $K_z >> K_x$ and $K_z >> K_y$. Using the potential given in Eq. (2.32b) for the ZOLZ reflections, Eq. (2.34) becomes

$$[\nabla_b^2 + 4\pi^2 U^{(0)}(\mathbf{b})]\Phi(\mathbf{b},z) \approx -4\pi i K_z \frac{\partial \Phi(\mathbf{b},z)}{\partial z} \tag{2.35}$$

Thus the solution of Eq. (2.35) can be directly written (Doyle and Berry, 1973) as

$$\Phi = \sum_j \varepsilon^j \exp(\zeta s_j z)\, \tau_j(\mathbf{b}) \tag{2.36a}$$

where

$$\zeta = \frac{i}{4\pi K_z} \tag{2.36b}$$

and $\tau_j(\mathbf{b})$ is a two-dimensional Bloch wave solution of

$$[\nabla_b^2 + 4\pi^2 U^{(0)}(\mathbf{b})]\tau_j(\mathbf{b}) = s_j \tau_j(\mathbf{b}) \tag{2.37}$$

The two-dimensional Bloch wave $\tau_j(\mathbf{b})$ satisfies the following orthonormal relation (Ashcroft and Mermin, 1976; also see Section 2.2.3):

$$\int d\mathbf{b}\, \tau_i^*(\mathbf{b})\tau_j(\mathbf{b}) = \delta_{ij} \tag{2.38}$$

Using the orthonormal relation of the C coefficients, it can be proved directly that

$$\sum_i \tau_i(\mathbf{b})\, \tau_i^*(\mathbf{b}') = \delta(\mathbf{b} - \mathbf{b}') \tag{2.39}$$

This means that $\{\tau_j(\mathbf{b})\}$ is a complete orthonormal function set. These are important relations that make it possible to expand an arbitrary convergent function in the representation of $\{\tau_j(\mathbf{b})\}$. This point is demonstrated in Section 10.3 for the solution of Green's function. Coefficients ε^j are determined by the boundary condition at $z = 0$. If the incident electron is described by $\Phi(\mathbf{b},0)$, the boundary condition requires

$$\Phi(\mathbf{b},0) = \sum_j \varepsilon^j \tau_j(\mathbf{b}) \tag{2.40}$$

Multiplying Eq. (2.40) by $\tau_i^*(\mathbf{b})$, integrating over $\mathbf{b}$, and using Eq. (2.38) yields

$$\varepsilon^i = \int d\mathbf{b}\, \Phi(\mathbf{b},0)\, \tau_i^*(\mathbf{b}) \tag{2.41}$$

At the exit face of the crystal slab $z = d$, the amplitude for electrons scattered to $\mathbf{u}$ in the two-dimensional reciprocal space is

$$A(\mathbf{u}) = \sum_j \varepsilon^j \exp(\zeta s_j d) \int d\mathbf{b} \exp(-2\pi i \mathbf{u}\cdot\mathbf{b})\, \tau_j(\mathbf{b}) \tag{2.42}$$

the intensity distribution $I = |A(\mathbf{u})|^2$.

Compared to the Bloch wave theory in reciprocal space (Section 2.2), the most important advantage of the real-space Bloch wave theory is that the diffraction of a finite incident electron probe of $\Phi(\mathbf{b},0)$ can be calculated without repeating the calculation for each plane wave component within the incident conical probe. This is convenient for the case of coherent convergent beam electron diffraction, in which disk overlaps may occur. The calculation of Bethe theory, however, has to be performed separately for individual incident plane wave components.

2.9.3. Effects of HOLZ Reflections

The HOLZ reflections can be included in this theory using the perturbation technique (Buxton, 1976; Vincent et al., 1984), in which the superposition coefficients of Bloch waves are assumed as z-dependent, i.e.,

$$\Phi = \sum_j \varepsilon^j(z) \exp(\zeta s_j z)\, \tau_j(\mathbf{b}) \tag{2.43}$$

and the upper layer potential $U^{(H)}$ is treated as a perturbation. This approach is exactly equivalent to the usual way of treating a time-dependent perturbation, in which z takes the place of time and the upper layer potential $U^{(H)}(\mathbf{b},z)$ represents the time-dependent perturbation. Substituting Eq. (2.43) into Eq. (2.5), the first- and second-order perturbation terms can be solved by the iteration method (for a review, see Bird, 1989).

2.10. DIFFRACTION CONTRAST IMAGES OF IMPERFECT CRYSTALS

Diffraction contrast imaging, a powerful technique for determining dislocation structures in crystals, is based on the following mechanism (Hirsch et al., 1977). The image is formed by selecting a single Bragg reflected beam using the objective aperture. The intensity of the Bragg beam is perturbed by the variation of local diffracting conditions due to the strain field of the dislocation. Thus this type of imaging is usually referred to diffraction contrast imaging.

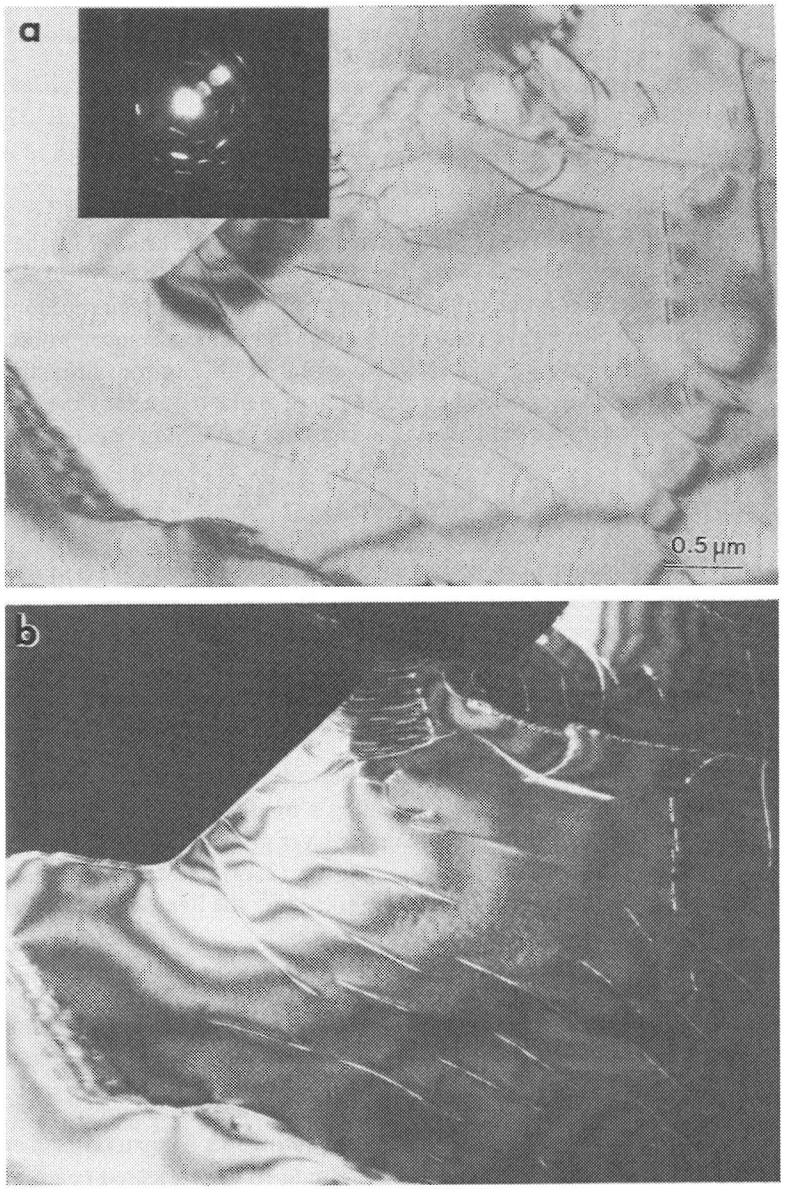

Figure 2.11. (a) Bright-field and (b) $\mathbf{g} = (20\bar{2}0)$ dark-field diffraction contrast images of polycrystalline α-Al_2O_3 recorded under the two-beam diffracting condition near [0001] zone. The insert is the diffraction pattern.

This section describes the basic theoretical approach for calculating the diffraction contrast of images. An excellent review has been given by Amelincks and Van Dyck (1993) on the fundamental theories of diffraction contrast imaging and associated applications.

Figure 2.11 shows the bright-field and dark-field diffraction contrast images of dislocations in a polycrystalline α-Al_2O_3 specimen. The dislocation lines are clearly resolved in both images. The intensity variation near dislocation lines results from dynamic diffraction from distorted lattices near dislocation cores. The contrast is due to the variation of the local diffracting condition, such as the excitation error, from that of perfectly structured lattices. The contrast is very sensitive to the nature of the dislocation, crystal orientation, incident beam direction, and crystal thickness. Therefore dynamic simulations are usually necessary if we intend to study detailed lattice distortion near the dislocations. But, as shown at the end of Section 2.10.4, no simulation is needed if we are interested only in determining the Burgers vector of dislocations. We now consider the theoretical approach for simulating diffraction contrast images.

2.10.1. Potential of Imperfect Crystals

In practice, atomic displacements can be introduced by defects, dislocations, or strain. For a general case, atom displacement may be described by a displacement vector $\mathbf{R}(\mathbf{r})$, which depends on the position of the atom. Thus the potential distribution in the crystal under the rigid-ion approximation is written as

$$U(\mathbf{r}) = \sum_n \sum_\alpha U_\alpha(\mathbf{r} - \mathbf{R}_n - \mathbf{r}_\alpha - \mathbf{R}(\mathbf{r})) \tag{2.44}$$

Using Eq. (1.17), the reciprocal lattice vector can be introduced as

$$\begin{aligned} U(\mathbf{r}) &= \sum_n \sum_\alpha \int d\mathbf{u}\, U_\alpha(\mathbf{u}) \exp\{2\pi i \mathbf{u}\cdot[\mathbf{r} - \mathbf{R}_n - \mathbf{r}_\alpha - \mathbf{R}(\mathbf{r})]\} \\ &= \sum_g \left[\sum_\alpha U_\alpha(\mathbf{g}) \exp\{-2\pi i \mathbf{g}\cdot[\mathbf{r}_\alpha + \mathbf{R}(\mathbf{r})]\}\right] \exp(2\pi i \mathbf{g}\cdot\mathbf{r}) \end{aligned} \tag{2.45}$$

The Fourier coefficient of the modified potential is

$$U_g(\mathbf{r}) = U_g \exp[-2\pi i \mathbf{g}\cdot\mathbf{R}(\mathbf{r})] \tag{2.46}$$

Therefore the distortion of the crystal lattice by defects introduces a position-dependent phase factor in the Fourier coefficient of the crystal potential.

2.10.2. Modified Bloch Wave Theory

For an imperfect crystal, the wave function usually does not obey the Bloch theorem and cannot be expanded into a Fourier series. Alternatively the solution of the Schrödinger equation is written as (Hirsch et al., 1977; Takagi, 1962 and 1969; Howie and Basinski, 1968)

$$\Psi(\mathbf{r}) = \sum_g \phi_g(\mathbf{r}) \exp[2\pi i(\mathbf{K} + \mathbf{g} + \mathbf{S}_g)\cdot\mathbf{r}] \tag{2.47}$$

where $|(\mathbf{K} + \mathbf{g} + \mathbf{S}_g)| = K$ and $\mathbf{S}_g = S_g \hat{z}$ is the excitation error. Substituting Eqs. (2.45)– (2.47) into Eq. (2.5), we obtain

$$\sum_g \{\frac{1}{4\pi^2} \nabla^2\phi_g + \frac{i}{\pi}(\mathbf{K} + \mathbf{g} + \mathbf{S}_g)\cdot\nabla\phi_g + \sum_h \phi_h U_{g-h} \exp[2\pi i(\mathbf{h} - \mathbf{g})\cdot\mathbf{R}$$

$$+ 2\pi i(\mathbf{S}_h - \mathbf{S}_g)\cdot\mathbf{r}]\}\exp[2\pi i(\mathbf{K} + \mathbf{g} + \mathbf{S}_g)\cdot\mathbf{r}] = 0 \tag{2.48}$$

Providing that all terms in the curly bracket vary slowly with $\mathbf{r}$, $\mathbf{R}(\mathbf{r})$ does not change significantly in a lattice distance and the $\nabla^2\phi_g$ term is negligible in comparison with the term $(\mathbf{K} + \mathbf{g} + \mathbf{S}_g)\cdot\nabla\phi_g$, then we have

$$(\mathbf{K} + \mathbf{g} + \mathbf{S}_g)\cdot\nabla\phi_g \approx \pi i \sum_h \phi_h U_{g-h} \exp[2\pi i(\mathbf{h} - \mathbf{g})\cdot\mathbf{R} + 2\pi i(\mathbf{S}_h - \mathbf{S}_g)\cdot\mathbf{r}] \tag{2.49}$$

This is the basic equation of the modified Bloch wave theory. The left-hand side of Eq. (2.49) indicates that it is necessary to differentiate ϕ_g in the direction of $(\mathbf{K} + \mathbf{g} + \mathbf{S}_g)$. Equation (2.49) was first proposed by Takagi (1962 and 1969) and Taupin (1964) for approaching crystals with defects, dislocation, or strain, and it is thus called the T equation. To simplify this equation and make it useful in image calculation, we now discuss the column approximation.

2.10.3. Column Approximation

The column approximation is usually assumed in image simulations of defects and dislocations. Figure 2.12 illustrates the column approximation (Hirsch et al., 1977; Howie and Whelan, 1961). A dislocation is situated at D inside the foil. An electron wave is incident on the top surface. The dislocation line causes a displacement of an atom in the column along AB from its true position by an amount $\mathbf{R}$ that depends on its distance z from the upper surface. The column approximation amounts to assuming that the electron wave function at B is the same as that at the lower surface of a crystal of infinite lateral extension, with the same displacement $\mathbf{R}(z)$, depending only on z, and not on the position of the column. Such a crystal can be considered an assembly of thin crystal rods, each perfect but displaced

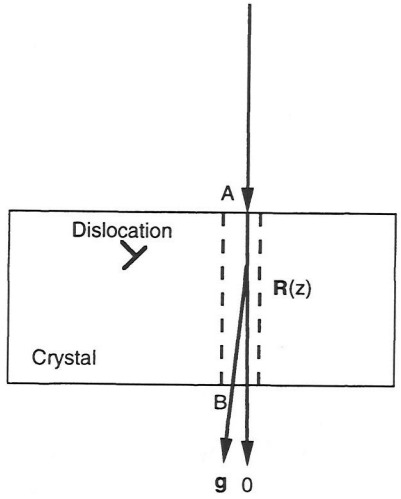

Figure 2.12. A column approximation used to calculate the diffraction contrast images of dislocations. The crystal is assumed to be composed of parallel columns. Within each column, the local lattice displacement $\mathbf{R}$ is assumed to depend only on z. The (x, y) dependence of $\mathbf{R}$ is introduced in calculations for different columns.

relative to each other. The wave function at the exit face of each column (or rod) depends only on the scattering of that column, so there is no interaction between columns. The width of the column is about 2 nm. This approximation may not be valid at dislocation cores where a rapid variation of $\mathbf{R}$ is possible. A rigorous discussion of the column approximation was given by Howie and Basinski (1968).

2.10.4. Howie–Whelan Equation

Contrast in dislocation images is produced by the variation of local crystal orientation due to the atom displacement $\mathbf{R}$. This results in the intensity variation of local reflected Bragg beams. This type of image can be simulated from column to column using full dynamic diffraction theory. The scattering of each column is equivalent to the scattering of a perfect crystal without considering the effects of its neighbor columns. In this case, ϕ_g is approximated to depend only on z. If the incident beam is along the z axis, so that

$$(\mathbf{K} + \mathbf{g} + \mathbf{S}_g)\cdot\nabla\phi_g, \approx K\frac{d\phi_g}{dz},$$

Eq. (2.49) becomes

$$\frac{d\phi_g}{dz} = \sum_h \frac{\pi i}{\xi_{g-h}} \phi_h \exp[2\pi i(\mathbf{h} - \mathbf{g})\cdot\mathbf{R} + 2\pi i(\mathbf{S}_h - \mathbf{S}_g)\cdot\mathbf{r}] \tag{2.50}$$

This is a many-beam equation for calculating the contrast of dislocations. Equation (2.50) can be solved exactly if there is no lattice distortion (i.e., $\mathbf{R} = 0$) (Van Dyck, 1976).

Under two-beam approximation, Eq. (2.50) reduces to the Howie–Whelan equation (Howie and Whelan, 1961),

$$\frac{d\phi_0}{dz} = \frac{\pi i}{\xi_0}\phi_0 + \frac{\pi i}{\xi_g}\phi_g \exp(2\pi i \mathbf{g}\cdot\mathbf{R} + 2\pi i \mathbf{S}_g\cdot\mathbf{r}) \tag{2.51a}$$

$$\frac{d\phi_g}{dz} = \frac{\pi i}{\xi_0}\phi_g + \frac{\pi i}{\xi_g}\phi_0 \exp(-2\pi i \mathbf{g}\cdot\mathbf{R} - 2\pi i \mathbf{S}_g\cdot\mathbf{r}) \tag{2.51b}$$

Equation (2.51a) and (2.51b) are the basic equation applied to simulate the diffraction contrast images. We now discuss the diffracting condition under which the contrast of dislocations disappears.

From Eq. (2.51), it is clear that the dislocation contrast disappears if $\mathbf{g}\cdot\mathbf{R} = 0$. For a general dislocation, the displacement vector $\mathbf{R}$ is directly related to the Burgers vector $\mathbf{b}_B$ and $\mathbf{b}_B \times \mathbf{u}_D$, where $\mathbf{u}_D$ is the direction of the dislocation line. In general, the reflected intensity of $\mathbf{g}$ is not affected if atom displacements are restricted to the reflecting plane of $\mathbf{g}$. Therefore diffracting conditions under which the contrast of dislocations disappears are

$$\mathbf{g}\cdot\mathbf{b}_B = 0 \qquad \mathbf{g}\cdot(\mathbf{b}_B \times \mathbf{u}_D) = 0$$

These are the general rules for determining the nature of dislocations in TEM. The condition $\mathbf{g}\cdot\mathbf{b}_B = 0$ means that atom displacements are restricted in the plane perpendicular to $\mathbf{g}$; thus no contrast is produced if the image is recorded using this Bragg reflection.

The Howie–Whelan equation [Eq. (2.51)] is the fundamental equation for simulating diffraction contrast images recorded under two-beam conditions. Figure 2.13 shows a comparison of the experimentally observed stacking fault images in TiAl for two different zone axes (Fig. 2.13a) with simulated images for stacking faults bounded by partial dislocations (Viguier et al., 1994). For TiAl, the majority of stacking faults and their bounding dislocations were observed to be completely out of contrast for $\mathbf{g} = [2\ 0\ \bar{2}]$ because $\mathbf{g}\cdot\mathbf{R} = 2n\pi$. For $\mathbf{g} = [2\ \bar{2}\ 0]$, however, the bounding partial dislocations were visible, but faults were invisible. These observations indicate that faults are lying in the (111) plane (i.e., $\mathbf{R} = \pm\ 1/3\ [111]$) and partial dislocations have a Burgers vector parallel to $\mathbf{g} = [1\ \bar{2}\ 1]$. Figure 2.13b is simulated for an extrinsic stacking fault with a double Schckley partial dislocation of $\mathbf{b}_B = 1/3\ [1\ \bar{2}\ 1]$. Simulated fault images corresponding to intrinsic stacking faults and extrinsic stacking faults (without partial dislocations) are shown in Fig. 2.13c–e. The best fit is found in Fig. 2.13b. Thus the stacking fault is

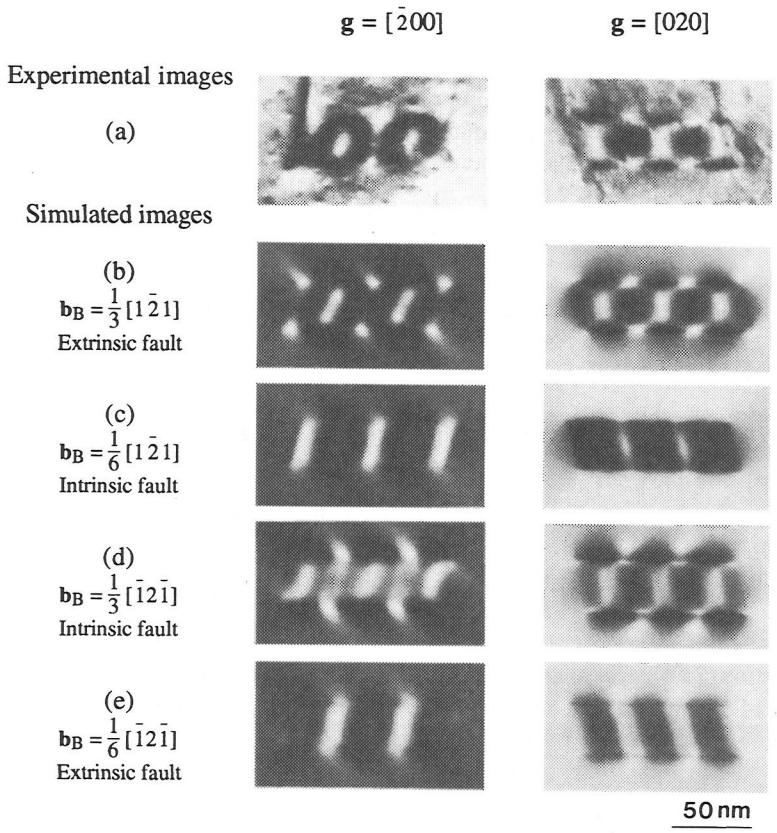

Figure 2.13. (a) Experimental bright-field images of a stacking fault dipole in TiAl recorded under two-beam diffracting conditions of $\mathbf{g} = [\bar{2}00]$ (*left-hand column*) and $\mathbf{g} = [020]$ (*right-hand column*); (b) simulated for an extrinsic stacking fault with a partial dislocation of $\mathbf{b}_B = 1/3\ [1\ \bar{2}\ 1]$. (c)–(e) Simulated images for extrinsic (without bounding dislocations) and intrinsic stacking faults under identical diffracting conditions: foil normal $\mathbf{n} = [2\ \bar{1}\ 4]$, $d = 115$ nm, beam direction $\mathbf{B} = [019]$ and $S_g = 0.006$ nm^{-1} for $\mathbf{g} = [\bar{2}00]$; $\mathbf{B} = [506]$ and $S_g = 0.019$ nm^{-1} for $\mathbf{g} = [020]$. The best fit is found in (b). (Courtesy of Viguier et al., 1994)

extrinsicand bounded by partial dislocations with Burgers vector $1/3\ [1\ \bar{2}\ 1]$. For simulations of electron diffraction contrast images of arbitrary displacement fields, the program package SIMCON provided by Janssens et al. (1992) could be very useful.

2.10.5. α Coefficient Method

We now introduce an alternative treatment of electron diffraction in the distorted crystals under the column approximation. This approach is applied in Section 2.11 to calculate the contrast of weak beam images. We first write the solution of the Schrödinger equation as

$$\Psi(\mathbf{r}) = \sum_i \alpha^{(i)}(z) \sum_g C_g^{(i)} \exp[2\pi i(\mathbf{K}+\mathbf{g})\cdot\mathbf{r} + 2\pi i \nu_i z] \exp(-2\pi i \mathbf{g}\cdot\mathbf{R}) \quad (2.52)$$

This theory is expressed in the form of Bloch wave coefficients, which are assumed to depend only on z, based on the column approximation. The comparison of Eq. (2.52) with Eq. (2.47) yields

$$\phi_g(\mathbf{r}) = \sum_i \alpha^{(i)}(z)\, C_g^{(i)} \exp[-2\pi i \mathbf{S}_g\cdot\mathbf{r} + 2\pi i \nu_i z] \exp(-2\pi i \mathbf{g}\cdot\mathbf{R}) \quad (2.53)$$

Substituting this equation into Eq. (2.50) and using Eqs. (2.13) and (2.16), we obtain

$$\frac{d\alpha^{(j)}(z)}{dz} = 2\pi i \sum_i \alpha^{(i)}(z) \exp[2\pi i(\nu_i - \nu_j)z] \sum_g C_g^{(i)} C_g^{(j)*} \frac{d(\mathbf{g}\cdot\mathbf{R})}{dz} \quad (2.54)$$

Equation (2.54) represents the change in amplitude of the jth Bloch wave in a crystal slice of thickness dz at a depth z, due to the change of local orientation. This theory is more convenient for calculating the weak beam image.

2.11. WEAK-BEAM IMAGING

As illustrated in the last section, the contrast of dislocation lines is determined by the magnitude of the local lattice distortion, and the image resolution is no better than 2 nm. The resolution of diffraction contrast images may be improved in the dark-field images recorded by using weak diffracted beams (Cockayne et al., 1969). A simple qualitative description of the weak-beam imaging technique follows. If a perfect crystal is oriented at the exact Bragg position, the corresponding diffracted beam is strong (unless the crystal thickness happens to be an integer multiple of the extinction distance). As the crystal is tilted away from the Bragg position, the intensity in the diffracted beam decreases, so that the beam becomes a weak beam. If the crystal contains a dislocation, lattice planes around the dislocation are locally tilted, and hence some of these planes may locally be tilted back into the Bragg position, as shown in Fig. 2.14. If this is the case, locally scattered intensity from perfect crystal regions is weak, but intensity scattered locally from the region satisfying the Bragg condition is strong (Hirsch et al., 1977).

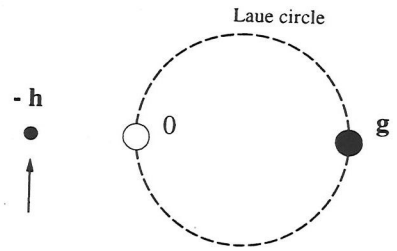

Figure 2.14. The three-beam diffracting condition for weak-beam imaging.

Figure 2.15b shows a weak-beam image of the same specimen area in Fig. 2.11. It is apparent that the dislocation lines are much thinner than those appearing in either the bright-field or the dark-field images in Fig. 2.11. The grain boundaries, which are hardly seen in the bright-field image, are clearly resolved in the weak beam image. There appears to be much less dynamic diffraction effect in the weak-beam image.

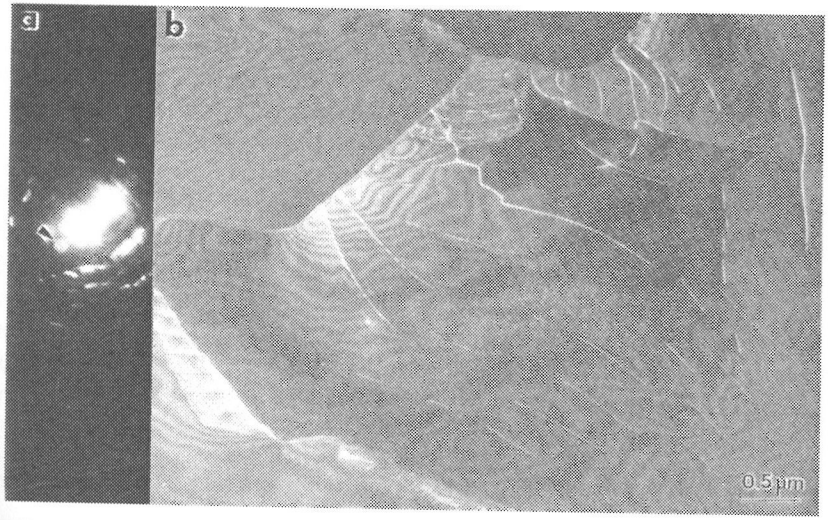

Figure 2.15. (a) Three-beam electron diffracting condition for recording the dark-field weak-beam image, shown in (b), of the polycrystalline α-Al_2O_3 specimen used for Fig. 2.11. The beak used for forming the weak-beam image is indicated by an arrowhead.

The weak-beam image is usually taken using a weak **–h** beam when a **+g** beam is set at Bragg condition (Fig. 2.14). We now use Eq. (2.54) to illustrate the dynamic description of weak-beam imaging of imperfect crystals,

$$\frac{d\alpha^{(j)}(z)}{dz} = \sum_i \alpha^{(i)}(z) \exp(2\pi i \Delta v_{ij} z) \frac{dR^{ij}(z)}{dz} \tag{2.55}$$

where

$$R^{ij}(z) = 2\pi i \sum_g C_g^{(i)} C_g^{(j)*} \mathbf{g}\cdot\mathbf{R} \qquad \Delta v_{ij} = v_i - v_j \tag{2.56}$$

Using Eq. (2.55), we perform the following mathematical operation (Cockayne, 1972):

$$\int_0^d dz \frac{d}{dz} \alpha^{(j)}(z) \exp[R^{ij}(z)]$$

$$= \int_0^d dz \sum_{i\neq j} \alpha^{(i)}(z) \frac{dR^{ij}(z)}{dz} \exp[2\pi i \Delta v_{ij} z - R^{ij}(z)] \tag{2.57}$$

Integrating the left-hand side of this equation, we obtain

$$\alpha^{(j)}(d) = \exp[R^{ij}(d)] \times$$

$$\{\int_0^d dz \sum_{i\neq j} \alpha^{(i)}(z) \frac{dR^{ij}(z)}{dz} \exp[2\pi i \Delta v_{ij} z - R^{ij}(z)] + \alpha^{(j)}(0)\} \tag{2.58}$$

The purpose of the preceding mathematical operation is to exclude the contribution of the terms with $i = j$. The first-order solution of Eq. (2.58) is obtained by taking $\alpha^{(i)} \approx C_0^{(i)*}$ on the right-hand side; thus

$$\alpha^{(j)}(d) \approx \exp[R^{ij}(d)] \times$$

$$\{\sum_{i\neq j} C_0^{(i)*} \int_0^d dz \frac{dR^{ij}(z)}{dz} \exp[2i\pi i \Delta v_{ij} z - R^{ij}(z)] + C_0^{(j)*}\} \tag{2.59}$$

If $dR^{ij}(z)/dz$ is a slow-variation function of z, the magnitude of $\alpha^{(j)}(d)$ depends approximately on

$$\int_0^d dz \exp[2\pi i \Delta v_{ij} z - R^{ij}(z)].$$

The integral is maximum when $[2\pi i \Delta v_{ij} z - R^{ij}(z)]$ is constant (Cockayne, 1972) or in an equivalent form

$$2\pi i \Delta v_{ij} - \frac{dR^{ij}(z)}{dz} = 0$$

or

$$v_j - v_i + \sum_g C_g^{(i)} C_g^{(j)*} \frac{d(\mathbf{g}\cdot\mathbf{R})}{dz} = 0 \tag{2.60}$$

Under the two-beam approximation, this condition becomes (Cockayne, 1972)

$$S_g + \frac{d(\mathbf{g}\cdot\mathbf{R})}{dz} = 0 \tag{2.61a}$$

This is the condition for dislocations to show bright contrast in a weak-beam image. This relation simply means that the local orientation variation has to reduce the excitation error of the **g** beam to satisfy the Bragg condition. For imperfect crystals and under the column approximation, the effective local excitation error is given by

$$S_g^{(eff)} = S_g + \frac{d(\mathbf{g}\cdot\mathbf{R})}{dz}$$

The condition $S_g^{(eff)} = 0$ means that the local region satisfies the Bragg condition, thus giving strong reflection intensity.

The column approximation was assumed in weak-beam imaging theory. However the large scattering angle between **–h** and **g** reflections shown in Fig. 2.14 could significantly increase the width of the column in some cases (Howie and Sworn, 1970; Lewis and Villagrana, 1979), resulting in incorrect positions of the dislocation contrast. It is thus necessary to examine each individual case carefully.

As just pointed out, the weak-beam image is formed due to the variation of the excitation error w with the local orientation. The dynamic diffraction effect in the **–h** beam is greatly reduced due to strong excitation of the **g** beam. For crystals containing grain boundaries, dislocations at interfacial regions are best seen in the weak-beam image; Fig. 2.16 shows such an example. The grain boundary is hardly seen in the bright-field image (Fig. 2.16a); it becomes relatively easy to see the interfacial dislocations in the dark-field diffraction contrast image (Fig. 2.16b). The fine details of dislocation are clearly seen in the weak-beam image (Fig. 2.16c), but the quantitative interpretation of the contrast is rather difficult.

Weak-beam imaging is best suited for imaging dislocations, but it is almost impossible to apply it to determine the nature of dislocations. The two-beam diffraction contrast images are very useful for determining the Burgers vector of dislocations.

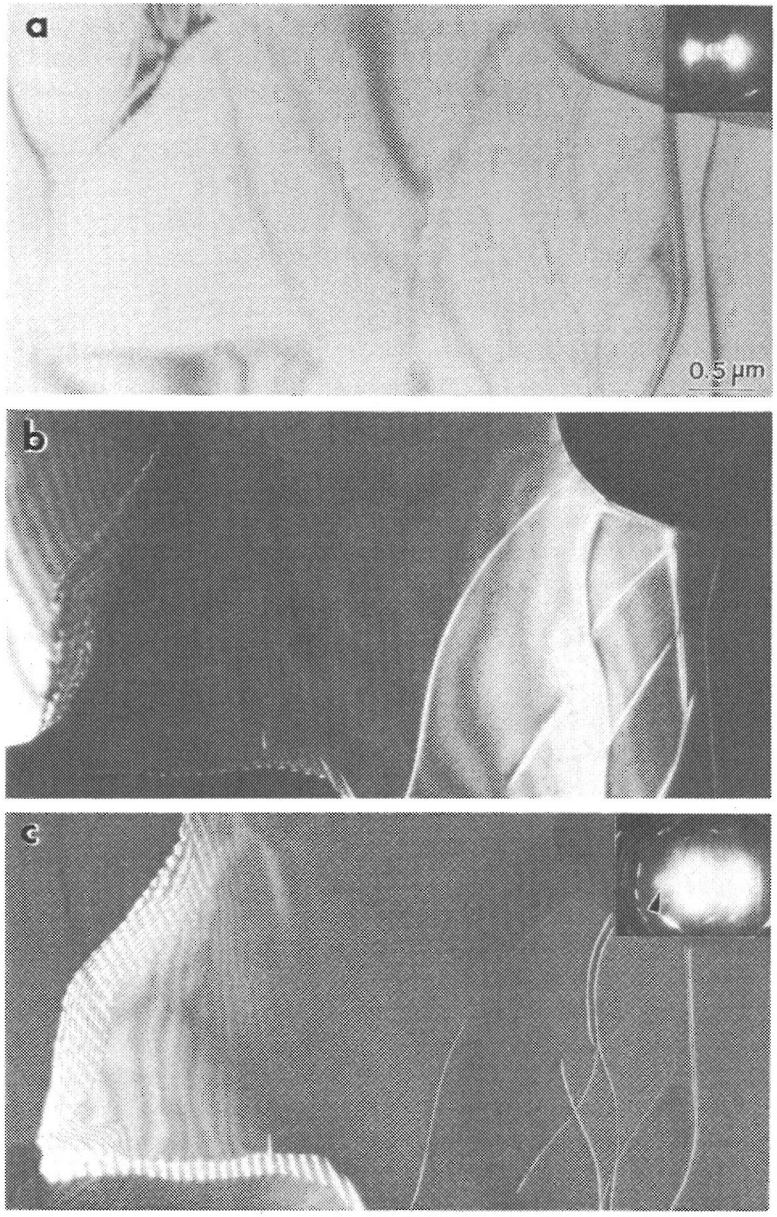

Figure 2.16. (a) Bright-field, (b) $\mathbf{g} = (20\bar{2}0)$ dark-field, and (c) weak-beam images of a polycrystalline α-Al_2O_3 specimen showing the advantages of the weak-beam technique for imaging interface dislocations. The beam used to form the weak-beam image is indicated by an arrowhead.

2.12. Absorption Effect in Dynamical Calculations

Interaction between the incident electron and the crystal is quite complex. Besides elastic scattering, inelastic excitations, such as X-ray emission, photon emission, and atom ionization, are usually involved. For thin crystals, the probability of inelastic scattering is usually small. As shown in Chapter 6, inelastic scattering of electrons is equivalent to introducing an imaginary potential into the elastic-scattering equation. This is usually known as the absorption effect. In the Bloch wave picture, taking the two-beam case as an example, one Bloch wave is a maximum between the columns of the atomic row, and the other Bloch wave is a maximum on the atomic rows (see Fig. 2.4). It is thus expected that the former is weakly scattered or absorbed and the latter will be strongly scattered or absorbed due to different inelastic-scattering processes. This is the so-called anomalous absorption effect. We can include absorption by replacing $V(\mathbf{r})$ with $V(\mathbf{r}) + i\,V'(\mathbf{r})$. In general, $|V(\mathbf{r})| >> |V'(\mathbf{r})|$, so we can use the first-order perturbation method to estimate the effect of absorption. The perturbation iV' results in a change ΔE in the energy of the Bloch wave B_i given by

$$\Delta E = \int d\mathbf{r}\, B_i^*(\mathbf{r})\,[-ieV'(\mathbf{r})]\,B_i(\mathbf{r}) \tag{2.61b}$$

The change in energy is equivalent to a change in K. Adding an iU'_{g-h} term in Eq. (2.13), we have

$$2KS_gC_g + \sum_{g\neq h} U_{g-h}C_h = 2K_z\nu C_g - i\sum_{g\neq h} U'_{g-h}\,C_h$$

This is equivalent to adding an imaginary component in the wave vector along the z direction. Thus the perturbation effect to the electron wave vector is

$$\Delta K_z = i\nu_i' = -\frac{m_e\Delta E}{h^2K_z} = \frac{m_e i}{h^2K_z}\int d\mathbf{r}\, B_i^*(\mathbf{r})\,[eV'(\mathbf{r})]\,B_i(\mathbf{r})$$

Using the Bloch wave expression in Eq. (2.17), the final calculation gives (Humphreys, 1979)

$$\nu_i' = \frac{1}{2K_z}\sum_g\sum_h C_g^{(i)*}\,U'_{g-h}\,C_h^{(i)} \tag{2.62}$$

Hence ν_i' is the imaginary part of the wave vector for the ith Bloch wave, and it can easily be calculated from the eigenvectors and the U' matrix. The following substitutions are thus made:

$$\nu_i \rightarrow \nu_i + i\nu_i' \tag{2.63a}$$

$$U_g \rightarrow U_g + iU_g' \tag{2.63b}$$

$$\frac{1}{\xi_g} \rightarrow \frac{1}{\xi_g} + \frac{i}{\xi_g'} \tag{2.63c}$$

with $\xi_g' = K/U_g'$. This is the phenomenological treatment of the absorption effect in electron diffraction. The calculation of the imaginary potential is illustrated in Chapter 6.

2.13. SUMMARY

As a summary of this chapter, we have introduced the Bloch wave theories and their applications in electron diffraction and imaging. The Bethe theory is powerful particularly because of its physical insight for evaluation of the contribution of different Bloch waves. This theory is much more convenient for sophisticated analytical expressions when there are only a few beams involved. The Bethe theory is best suited for CBED calculations in reciprocal space if there are no disk overlaps, but the calculations can be easily performed only for three-dimensional perfect crystals. Real-space Bloch wave theory is convenient for simulations of diffraction contrast images and CBED if there are disk overlaps. A detailed comparison of the Bethe theory with other theories, presented in the next few chapters, is given in Section 4.5.

3

Dynamic Elastic Electron Scattering II: Multislice Theory

For simulations of electron images, the Bloch wave approach is more convenient for dealing with these cases in which either the crystal contains no defects or the image resolution is so low that the column approximation holds. When the image resolution approaches the atomic level, the dominant contrast mechanism is phase contrast, and the effect of diffraction contrast is minimized. In this case, it is more convenient to apply the multislice theory, particularly when defects are present in the crystal. The most important advantage of the multislice theory is that it does not require three-dimensional periodicity of the crystal; thus images of interfaces, surfaces, and dislocations can be simulated. Chapter 3 outlines the theoretical scheme of the multislice theory and its applications. Methods to improve the theory are illustrated to include HOLZ reflections accurately.

3.1. PHYSICAL OPTICS APPROACH

The multislice many-beam dynamic electron diffraction theory of Cowley and Moodie (1957) was originally derived from the physical optics approach, in which electron transmission through a crystal is represented by transmission through a set of two-dimensional phase objects, as shown in Fig. 3.1. The crystal is cut into many slices of equal thickness Δz in the direction perpendicular or nearly perpendicular to the incident beam. This treatment is usually convenient if incident electrons are along one of the low-index zone axes. When slice thickness tends to be very small, the scattering of each slice can be based on the projected potential approximation. If the backscattering effect is negligible, the transmission of the electron wave through each slice can be considered a two-step process—the phase modulation of the wave by the projected atomic potential within the slice and the propagation of the modulated wave in a vacuum for distance Δz along the beam direction before striking the next crystal slice (Fig. 3.1). The projected potential approximation was